N-*V*–Diamond Magnetic Microscopy Using a Double Quantum 4-Ramsey Protocol

Connor A. Hart,[1,2,3,4,†] Jennifer M. Schloss,[5,6,7,†] Matthew J. Turner,[1,2,3,4,7] Patrick J. Scheidegger,[8] Erik Bauch,[9] and Ronald L. Walsworth[1,2,3,4,7,9,*]

[1] *Department of Physics, Harvard University, Cambridge, Massachusetts 02138, USA*
[2] *Department of Physics, University of Maryland, College Park, Maryland 20742, USA*
[3] *Department of Computer and Electrical Engineering, University of Maryland, College Park, Maryland 20742, USA*
[4] *Quantum Technology Center, University of Maryland, College Park, Maryland 20742, USA*
[5] *Lincoln Laboratory, Massachusetts Institute of Technology, Lexington, Massachusetts 02421, USA*
[6] *Department of Physics, Massachusetts Institute of Technology, Cambridge, Massachusetts 02139, USA*
[7] *Center for Brain Science, Harvard University, Cambridge, Massachusetts 02138, USA*
[8] *Department of Physics, ETH Zurich, Zurich, 8093, Switzerland*
[9] *Harvard-Smithsonian Center for Astrophysics, Cambridge, Massachusetts 02138, USA*

(Received 29 September 2020; accepted 3 March 2021; published 12 April 2021)

We introduce a double quantum (DQ) 4-Ramsey measurement protocol that enables wide-field magnetic imaging using nitrogen-vacancy (N-*V*) centers in diamond, with enhanced homogeneity of the magnetic sensitivity relative to conventional single quantum (SQ) techniques. The DQ 4-Ramsey protocol employs microwave-phase alternation across four consecutive Ramsey (4-Ramsey) measurements to isolate the desired DQ magnetic signal from any residual SQ signal induced by microwave pulse errors. In a demonstration experiment employing a 1-μm-thick N-*V* layer in a macroscopic diamond chip, the DQ 4-Ramsey protocol provides a volume-normalized dc magnetic sensitivity of $\eta^V = 34$ nT Hz$^{-1/2}$ μm$^{3/2}$ across a 125 μm $\times$ 125 μm field of view, with about 5$\times$ less spatial variation in sensitivity across the field of view compared to a SQ measurement. The improved robustness and magnetic sensitivity homogeneity of the DQ 4-Ramsey protocol enables imaging of dynamic broadband magnetic sources such as integrated circuits and electrically active cells.

DOI: 10.1103/PhysRevApplied.15.044020

I. INTRODUCTION

Nitrogen-vacancy (N-*V*) color centers in diamond constitute a leading quantum sensing platform, with particularly diverse applications in magnetometry [1]. The negatively charged N-V^- center has an electronic spin-triplet ground state with magnetically sensitive spin resonances, offers all-optical spin-state preparation and readout under ambient conditions, and can be engineered at suitably high densities in favorable geometries [2,3]. These properties make ensembles of N-V^- centers particularly advantageous for wide-field magnetic microscopy of physical and biological systems with micrometer-scale spatial resolution, a modality known as the quantum diamond microscope (QDM) [4]. QDM applications to date include imaging magnetic fields from remnant magnetization in geological specimens [5], domains in magnetic memory [6], iron mineralization in chiton teeth [7], current flow in graphene devices [8,9] and integrated circuits [10], populations of living magnetotactic bacteria [11], and cultures of immunomagnetically labeled tumor cells [12].

Despite this progress, QDM magnetic imaging applications have been largely restricted to mapping of static magnetic fields exceeding several microtesla due to the shortcomings of conventional single quantum (SQ) magnetometry. SQ schemes sense changes in the frequency or phase accumulation between two sublevels with difference in spin projection quantum number $\Delta m = 1$. In particular, the sensitivity of QDMs using continuous-wave optically detected magnetic resonance (cw-ODMR) is impaired by competing effects of the optical and microwave (MW) control fields applied during the sensing interval [3,4]. Pulsed-ODMR schemes, which separate the optical spin-state preparation and readout from the MW control and sensing interval, offer improved sensitivity but cannot exceed the performance achievable with SQ Ramsey magnetometry [3].

*walsworth@umd.edu
†These authors contributed equally to this work.

 © 2021 American Physical Society

Furthermore, any SQ magnetometry scheme is vulnerable to diamond-crystal stress inhomogeneities and temperature variations, which shift and broaden the N-V^- spin resonances. Such stress gradients are particularly pernicious for QDM applications, with typical gradient magnitudes comparable to N-V^- resonance line widths (0.1–1 MHz) and a spatial structure spanning the submicron to millimeter scales [13]. Stress-induced resonance shifts or broadening may be mistaken for magnetic signals of interest. Stress gradients can also degrade the per-pixel sensitivity and sensitivity homogeneity across an image. While protocols such as sequentially sampling the ODMR spectrum at multiple frequencies [5] or employing four-tone MW control [14,15] can separate magnetic and nonmagnetic signals, the worsened and inhomogeneous magnetic sensitivity caused by stress gradients remains unaddressed.

Here, we demonstrate a double quantum (DQ) 4-Ramsey protocol that overcomes the shortcomings of SQ cw- and pulsed-ODMR measurement techniques. This protocol expands upon the advantageous pulsed Ramsey scheme, which temporally separates the spin-state control, optical readout, and sensing intervals. The scheme thus enables the use of increased laser and MW intensity compared to cw-ODMR, allowing for improved measurement contrast and higher fluorescence count rates without broadening the N-V^- spin resonances. Furthermore, the protocol exploits the benefits of DQ coherence magnetometry, which leverages a double quantum superposition of the $m_s = |\pm 1\rangle$ ground-state sublevels, to cancel common-mode resonance shifts and broadening from stress, electric fields, and temperature variations [16–19]. This DQ Ramsey-based scheme can therefore disentangle magnetic and nonmagnetic signals while also enabling improved homogeneous per-pixel magnetic sensitivity across an image.

Previously, DQ Ramsey magnetic imaging has been hindered by the technical challenge of producing sufficiently uniform and strong MW fields to avoid spatially varying errors in the optimal MW pulses and hence the N-V^- measurement protocol. Such pulse errors result in a residual SQ coherence that remains sensitive to common-mode shifts of the $|\pm 1\rangle$ sublevels, degrading the robustness of DQ magnetometry to stress-induced shifts and temperature drifts.

The present work circumvents this challenge with a DQ 4-Ramsey protocol specifically designed to suppress the contribution of residual SQ coherence. By properly selecting the spin-1 rotations applied in four consecutive Ramsey measurements (4-Ramsey), the DQ signal from each Ramsey measurement is preserved while the residual SQ signals cancel. This scheme is broadly applicable to both N-V^- ensemble imaging and bulk-sensing modalities, simultaneously mitigating the pernicious effects of stress gradients and temperature-induced drifts. Since the 4-Ramsey protocol is a straightforward extension of established phase-alternation schemes, implementation in an existing system does not typically require additional MW components.

After describing the N-V^- center and experimental apparatus in Sec. II, we outline and experimentally demonstrate the DQ 4-Ramsey protocol (Sec. III). In Sec. IV, we use SQ and DQ Ramsey fringe imaging to characterize, pixel by pixel, the reduced spatial variation in T_2^* and the N-V^- resonance frequency when using the DQ sensing basis. Using the same field of view as in Sec. IV, we then measure a 1.5× improved median per-pixel sensitivity and a 4.7× narrower spatial distribution of per-pixel sensitivity using the DQ sensing basis compared to the SQ basis (Sec. V). In Sec. VI we highlight the next steps to further improve the dc magnetic sensitivity and temporal resolution, and we provide an outlook describing envisioned applications for high-sensitivity broadband magnetic microscopy using the DQ 4-Ramsey protocol.

II. EXPERIMENTAL METHODS

The N-V center is a C_{3v} symmetric color center in diamond formed by substitution of a nitrogen atom adjacent to a vacancy in the carbon lattice. We restrict our attention to the negatively charged N-V^- center, which has an electronic spin-triplet ($S = 1$) ground state with a zero-field splitting at room temperature of $D \approx 2.87$ GHz between the $|m_s = 0\rangle$ and $|m_s = \pm 1\rangle$ magnetic sublevels, as shown in Fig. 1(a). The application of an external magnetic field splits the $|\pm 1\rangle$ sublevels by the Zeeman effect. In the presence of a magnetic field $\vec{B}$ exceeding approximately 1 mT aligned with the N-V^- symmetry axis z, the N-V^- ground-state Hamiltonian can be approximated as [5,13,20–22]:

$$H/h \approx [D(T) + M_z]S_z^2 + \frac{\gamma}{2\pi}B_z S_z, \tag{1}$$

where S_z is the dimensionless spin-1 operator, M_z is the axial spin-stress coupling parameter, $D(T)$ is the temperature-dependent zero-field splitting, B_z is the projection of the external magnetic field $\vec{B}$ along the N-V^- symmetry axis, and $\gamma/(2\pi) = 28.03\ \mathrm{GHz\,T^{-1}}$ is the N-V^- gyromagnetic ratio. The transverse magnetic, transverse electric, and transverse crystal stress terms are neglected as motivated in Refs. [13,16,23] (for further discussion of the crystal stress terms, see the Supplemental Material [24]). Under these assumptions, the observed spatial variations in the N-V^- spin resonance frequencies and line widths are attributed to axial stress gradients arising from stress inhomogeneity in the host diamond crystal. Note that for DQ coherence magnetometry, the relative phase accumulated between the $|\pm 1\rangle$ sublevels is not only immune to common-mode energy level shifts [proportional to S_z^2

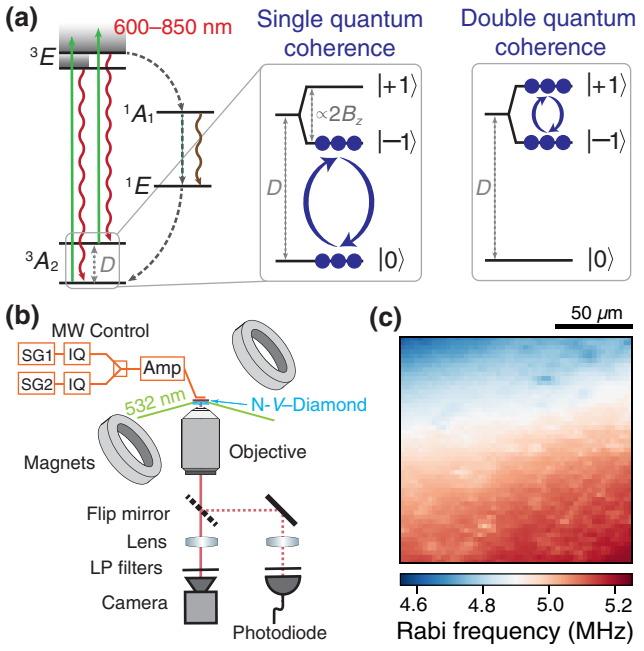


FIG. 1. The N-V^- energy-level diagram and the experimental apparatus. (a) The energy-level diagram for the negatively charged nitrogen vacancy (N-V^-) in diamond with zero-field splitting D between the ground-state spin levels $|m_s = 0\rangle$ and $|m_s = \pm 1\rangle$. The enlarged views depict single quantum (SQ) and double quantum (DQ) coherence. To induce a DQ coherence, the $|0\rangle \rightarrow |\pm 1\rangle$ spin transitions are simultaneously irradiated with a two-tone resonant microwave (MW) pulse. (b) An overview of the QDM apparatus, including 532-nm excitation of a micron-scale layer of N-V centers in a macroscopic diamond chip, using total internal reflection (TIR). N-V fluorescence is collected using a 20× objective onto a camera or photodiode. 647-nm and 532-nm long-pass (LP) optical filters partially isolate the N-V^- fluorescence from the background N-V^0 fluorescence. The MW control fields are synthesized using two signal generators with phase control on both tones and applied via a millimeter-scale shorted coaxial loop. A bias magnetic field of 5 mT is aligned with the N-V centers oriented along a single crystallographic axis. (c) Typical N-V^- Rabi frequency variation across a 125 μm × 125 μm field of view. The effects of inhomogeneous stress-induced N-V^- resonance shifts on the Rabi frequency are visible, in addition to a quasilinear Rabi gradient due to spatial variation in the MW amplitude.

in Eq. (1)] but also doubly sensitive to magnetic fields [16–18].

The present study employs a QDM to image spin-state-dependent fluorescence from a 1-μm-thick nitrogen-doped CVD diamond layer ($[N_{total}] \approx 20$ ppm, $^{12}C = 99.995\%$, natural abundance nitrogen) grown by Element Six Ltd. on a $(2 \times 2 \times 0.5)$ mm^3 high-purity diamond substrate. Postgrowth treatment via electron irradiation and annealing increases the N-V^- concentration in the nitrogen-doped layer to approximately 2 ppm. The magnitude and distribution of stress inhomogeneity in the selected sample is representative of typical diamonds fabricated for N-V–based magnetic imaging (for additional examples, see Refs. [13,25]).

An approximately 150 μm by 300 μm region of the N-V layer is illuminated with 1 W of 532 nm laser light in a total internal reflection (TIR) geometry [see Fig. 1(b)] and the associated N-V^- fluorescence is collected onto either a Heliotis heliCam C3 camera or a Hamamatsu C10508 avalanche photodiode. The heliCam operates by subtracting alternate exposures in analog and then digitizing the resultant background-subtracted signal. This procedure enables the detected magnetic-field-dependent N-V^- fluorescence to fill the 10-bit dynamic range of each pixel for modulated magnetometry sequences synchronized with the camera exposures. With an external frame rate of up to 3.8 kHz, the heliCam provides submillisecond temporal resolution, while the internal exposure rate of up to 1 MHz enables the accumulation of signal from multiple Ramsey measurements, each a few microseconds in duration, per external frame (see the Supplemental Material [24]). Two signal generators with phase control synthesize the dual-tone MW fields required for DQ coherence magnetometry in the presence of a bias magnetic field (Appendix A). Control over the relative phase between the two MW tones enables selective coupling to different DQ superposition states as described in the following section. These MW fields are applied to the N-V ensemble using a millimeter-scale shorted coaxial loop. Figure 1(c) depicts the typical spatial variation in Rabi frequency.

III. DQ 4-RAMSEY MEASUREMENT PROTOCOL

We introduce a measurement protocol consisting of four consecutive Ramsey sequences that, when combined, isolate the desired DQ magnetometry signal from residual SQ signal by modulating the MW pulse phases. SQ protocols commonly employ sets of two Ramsey sequences (2-Ramsey), alternating the phase of the final $\pi/2$ pulse in successive sequences by 180°, to modulate the N-V^- fluorescence and cancel low-frequency noise, such as $1/f$ noise [26]. In such a SQ 2-Ramsey protocol, the magnetometry signal alternately maps to positive and negative changes in N-V^- fluorescence, such that the subtraction of every second detection from the previous yields a rectified magnetometry signal [see Fig. 2(a)].

Analogous DQ 2-Ramsey protocols exist: two-tone MW pulses couple the $|0\rangle$ state to equal-amplitude superpositions of the $|\pm 1\rangle$ states, with a phase relationship $(|+1\rangle + e^{i\Delta\phi}|-1\rangle)/2$ determined by the relative phase $\Delta\phi$ between the two MW tones [17]. By modulating $\Delta\phi = \{0°, 180°\}$ between the tones in the final $\pi/2$ pulse, the $|0\rangle$ state can be alternately coupled to the orthogonal superposition states $|\pm DQ\rangle = (|+1\rangle \pm |-1\rangle)/\sqrt{2}$. Figure 2(b) depicts a representative DQ 2-Ramsey protocol.

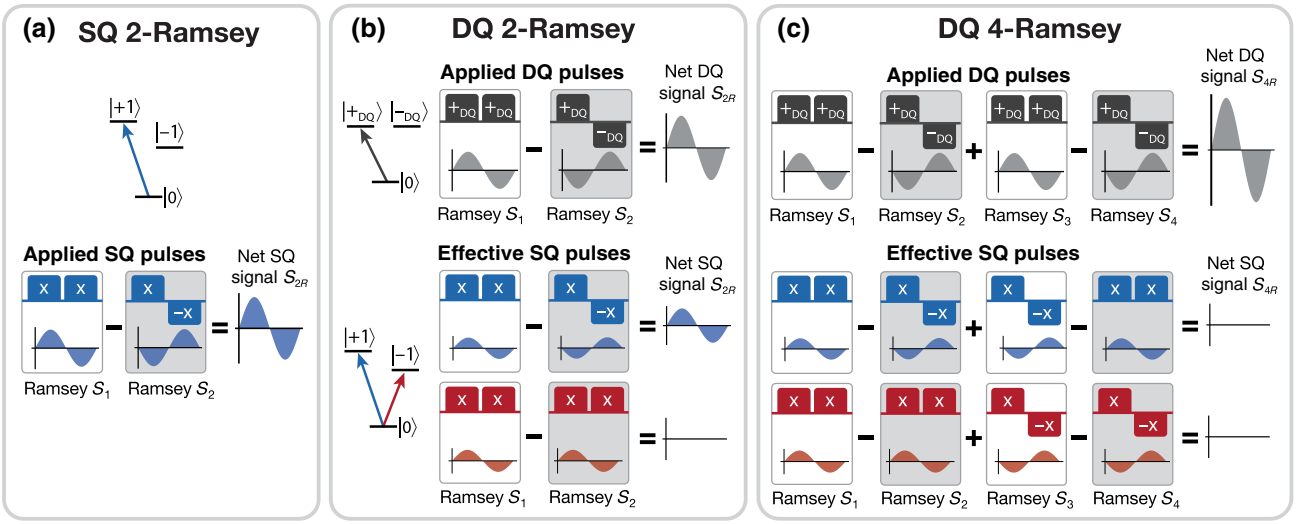


FIG. 2. The 2-Ramsey and 4-Ramsey measurement protocols. (a) A representation of the single quantum (SQ) 2-Ramsey protocol. The choice of phases and the resultant dc-magnetometry signals are shown for each Ramsey sequence. The single-tone MW pulses address only the $|0\rangle \rightarrow |+1\rangle$ spin resonance. (b) A representation of the double quantum (DQ) 2-Ramsey protocol. In the top row (gray), the two-tone DQ pulses applied during each Ramsey sequence are depicted above the dc-magnetometry curve associated with that choice of phases. The net DQ magnetometry signal S_{2R} is shown on the right. In the middle and bottom rows, the applied MW pulses are decomposed into effective SQ rotations for each pseudo-two-level system. Note that the SQ signals produced by the effective pulses addressing the $|0\rangle \rightarrow |+1\rangle$ transition (blue) do not cancel. As a result, SQ signals corrupt the resultant DQ 2-Ramsey signal when residual SQ coherence is present. (c) A representation of the DQ 4-Ramsey measurement protocol to cancel residual SQ signals resulting from MW pulse errors. The net DQ magnetometry signal S_{4R} is shown on the right. In the presence of pulse errors, the resultant SQ dc-magnetometry signals for each Ramsey sequence are depicted and shown to produce no net SQ signal when combined according to Eq. (2).

Although DQ 2-Ramsey protocols effectively cancel noise at frequencies below the phase-modulation frequency, this does not disentangle the desired DQ signal from the unwanted SQ signal arising from MW pulse errors. In N-V^- ensemble measurements, MW pulse errors commonly arise from spatial gradients in the Rabi frequency across an interrogated ensemble or field of view, see Fig. 1(c) for an example of the typical Rabi gradient produced by a millimeter-scale shorted coaxial loop. Although the spatial properties of the MW control field depend upon setup-specific MW synthesis and delivery approaches, the 4-Ramsey protocol universally relaxes requirements on MW-field uniformity. The hyperfine splitting of the N-V^- resonances and stress-induced N-V^- resonance shifts can also introduce MW pulse errors via the detuning-dependent effective Rabi frequency. In this work, errors induced by the hyperfine splitting (2.2 MHz between each of the $m_I = \{-1, 0, +1\}$ ^{14}N nuclear spin states) are comparable to the Rabi gradient of ± 200 kHz and are uniform across the field of view. In addition, the spatially correlated Rabi frequency variations on the 1–10 μm length scales in Fig. 1(c) are attributed to stress-induced shifts on the order of hundreds of kilohertz (see Sec. IV and the Supplemental Material [24]).

We now describe the phase-alternation pattern used in the DQ 4-Ramsey protocol to isolate DQ magnetic signals, and we present an experimental demonstration using photodiode-based measurements. Figure 2(c) depicts the resulting DQ rotations applied in the $\{|0\rangle, |-\mathrm{DQ}\rangle, |+\mathrm{DQ}\rangle\}$ basis for a particular implementation of the DQ 4-Ramsey protocol, where the choice of relative phases is restricted to 0° or 180° (generalized phase requirements can be found in the Supplemental Material [24]). While the initial pulse in each Ramsey sequence prepares the $|+\mathrm{DQ}\rangle$ state, the final pulse alternately couples to the $|+\mathrm{DQ}\rangle$ and $|-\mathrm{DQ}\rangle$ states, similar to the DQ 2-Ramsey protocol. If the signal from each of the four measurements $i = 1 - 4$ is denoted by S_i then the rectified DQ signal S_{4R} is given by

$$S_{4R} = S_1 - S_2 + S_3 - S_4, \tag{2}$$

where, as shown in Fig. 2(c), S_2 and S_4 contain DQ signals with opposite sign compared to S_1 and S_3. When implementing these DQ rotations, we have flexibility in choosing the absolute phases of each tone. For example, $\{0^\circ, 0^\circ\}$ and $\{180^\circ, 180^\circ\}$ both couple to $|+\mathrm{DQ}\rangle$ while $\{0^\circ, 180^\circ\}$ and $\{180^\circ, 0^\circ\}$ couple to $|-\mathrm{DQ}\rangle$. We leverage this degree of freedom to ensure that residual SQ signals are canceled by Eq. (2). The effective SQ pulses applied to each two-level subsystem transition ($|0\rangle \rightarrow |+1\rangle$ and

$|0\rangle \rightarrow |-1\rangle$) are illustrated in Fig. 2(c) as Bloch-sphere rotations about the axes x and $-x$.

If pulse errors arise, leading to residual SQ coherence, then the resultant SQ signal contained in the summation $S_2 + S_4$ is the same as $S_1 + S_3$ (so long as the errors are constant over the approximately 10 μs measurement duration). By subtracting these summations, S_{4R} from Eq. (2) eliminates this spurious SQ signal. When using the heliCam, Eq. (2) is physically implemented by the on-chip circuitry, which subtracts alternating exposures in analog before digitization. For photodiode-based measurements, which provide access to S_{1-4} directly, the right-hand side of Eq. (2) can be divided by the sum of S_{1-4} to cancel the effects of multiplicative noise sources such as laser-intensity fluctuations.

Figure 3 illustrates the benefit of the DQ 4-Ramsey protocol over SQ and DQ 2-Ramsey protocols. The measured changes in contrast in response to differential (magnetic-field-like) and common-mode (temperature, axial-stress-like) shifts are compared when operating with a

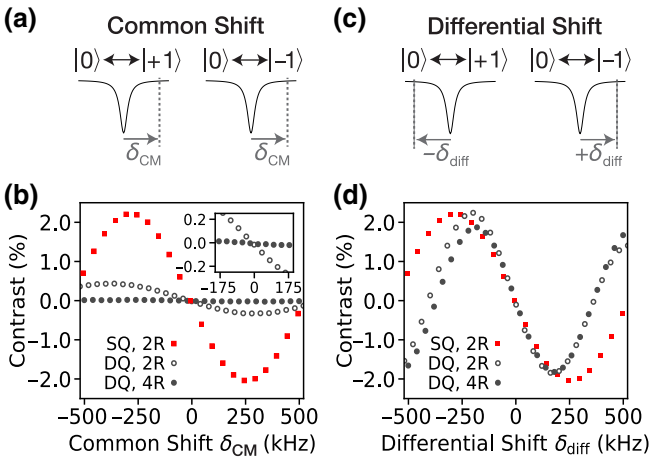


FIG. 3. The measured response to common-mode and differential detunings. (a) A depiction of the applied MW-field frequencies detuned from the N-V^- resonances in common mode by δ_{CM} to emulate stress- and temperature-induced shifts. (b) Single-channel (photodiode) measurements of the N-V^- response to common-mode shifts of the $|0\rangle \rightarrow |-1\rangle$ and $|0\rangle \rightarrow |+1\rangle$ spin resonances. For each sensing protocol, $\delta_{CM} = 0$ indicates the point of maximum slope after calibration (see Appendix B). The SQ 2-Ramsey response, addressing only the $|0\rangle \rightarrow |+1\rangle$ spin resonance, is included for reference. The DQ 4-Ramsey response to common-mode shifts is suppressed by 96× compared to the SQ 2-Ramsey shift response. (c) A depiction of the applied MW-field frequencies detuned from the N-V^- resonances differentially by $\pm\delta_{diff}$ to emulate axial-magnetic-field-induced shifts. (d) Single-channel measurements of the N-V^- response to differential shifts of the $|0\rangle \rightarrow |-1\rangle$ and $|0\rangle \rightarrow |+1\rangle$ spin resonances. For each measurement protocol, $\delta_{diff} = 0$ indicates the point of maximum slope after calibration, which determines the optimal magnetometer sensitivity. The SQ 2-Ramsey response, addressing only the $|0\rangle \rightarrow |+1\rangle$ spin resonance, is included for reference.

free-precession interval τ and detuning from the center hyperfine resonance, optimized for magnetic sensitivity (see Appendix B). For the data presented in Fig. 3, N-V^- fluorescence from the same field of view as shown in Fig. 1(c) is collected onto a photodiode while sweeping the applied MW tone(s). By approximating the change in fluorescence about the optimal detuning ($\delta_{CM} = \delta_{diff} = 0$) using a linear fit, we find that DQ Ramsey measurements using the conventional 2-Ramsey protocol (with residual SQ signal) suppress the response to common-mode shifts δ_{CM} compared to SQ 2-Ramsey measurements by a factor of 7. Although this suppression factor depends on both the particular setup and diamond, the factor of 7 reported in this work is similar to that in Ref. [18] for a single N-V^-, which also attributes the residual observed response to MW pulse imperfections. Meanwhile, under the same experimental conditions, the DQ 4-Ramsey protocol suppresses the common shift response by about a factor of 100 compared to SQ Ramsey measurements. The residual DQ 4-Ramsey protocol response to common-mode shifts, visible in the inset of Fig. 3(b), is attributed to experimental imperfections when manipulating the phase of the MW control pulses. Alternative hardware implementations (e.g., using an arbitrary waveform generator) could likely yield further suppression of the DQ 4-Ramsey protocol response to common-mode shifts.

As depicted in Fig. 3(d), the DQ 4-Ramsey and DQ 2-Ramsey responses exhibit about a cumulative 25% increase in slope (and an associated improvement in magnetometer sensitivity) compared to the SQ 2-Ramsey response, after accounting for the increased effective gyromagnetic ratio in the DQ basis and the loss of DQ contrast due to pulse errors. When each Ramsey signal S_i is accessible, the bandwidth of the 4-Ramsey measurement is approximately half the bandwidth of the 2-Ramsey measurement. However, there is no corresponding decrease in sensitivity because the acquired DQ magnetic signals add constructively across the 4-Ramsey protocol (see the Supplemental Material [24]).

IV. RAMSEY FRINGE IMAGING

We employ SQ 2-Ramsey and DQ 4-Ramsey measurements to image the N-V^- ensemble spin properties relevant for dc-magnetic-field sensitivity across a 125 μm by 125 μm field of view. The photon-shot-noise-limited sensitivity of a Ramsey-based measurement η_{ramsey} depends upon the N-V^- ensemble dephasing time T_2^*, the contrast C, and the average number of photons collected per measurement N [3]:

$$\eta_{ramsey} = \frac{1}{\gamma}\frac{1}{\Delta m}\frac{1}{Ce^{-(\tau/T_2^*)^p}\sqrt{N}}\frac{\sqrt{\tau + t_{r,i}}}{\tau}, \qquad (3)$$

where Δm accounts for the difference between the m_s states used for the sensing basis ($\Delta m = 1, 2$ for the SQ, DQ

bases), τ is the free-precession interval per measurement, p describes the decay shape, and $t_{r,i}$ indicates the time duration dedicated to readout and initialization per measurement. The optimal free-precession interval is determined by the N-V^- ensemble dephasing time T_2^*, which is proportional to the inverse of the inhomogeneous line width Γ ($T_2^* = 1/\pi\Gamma$, assuming a Lorentzian line shape). Axial stress gradients within a pixel degrade η_{ramsey} by decreasing T_2^*; stress-induced resonance shifts across an image both worsen η_{ramsey} by ensuring that the chosen MW frequency is suboptimal for all but a subset of pixels and introduce spatially varying nonmagnetic offsets in the Ramsey signal that can complicate data analysis [13].

We image the N-V^- ensemble spin properties by sweeping the free-precession time in the SQ and DQ Ramsey sequences and fitting the fringes to a sum of oscillations with a common decay envelope:

$$S_{\text{ramsey}}(\tau) = e^{-\tau/T_2^*} \sum_{i=m_I} A_i \sin(2\pi f_i + \delta_i), \tag{4}$$

where each oscillatory term, indexed by $m_I = \{-1, 0, 1\}$ (for an ^{14}N ensemble), has an amplitude A_i, a frequency f_i, a phase shift δ_i, and a decay shape fixed to $p = 1$ [16]. A purposeful detuning of 3 MHz from the resonance corresponding to the $m_I = 0$ hyperfine population is introduced in order to more easily extract all three frequencies and the decay envelope. Equation (4) is rapidly fitted to the data pixel by pixel using the open-source GPU-accelerated nonlinear least-squares fitting software package GPUfit [27]. The typical 95% confidence intervals (C.I.) for the extracted dephasing times T_2^* and amplitudes A_i discussed below are less than 5%, while the typical C.I. for f_i are about 0.5%.

A. Dephasing times

The extracted T_2^* values for the SQ and DQ sensing bases are shown as images in Figs. 4(a) and 4(b) and plotted as a histogram in Fig. 4(c). To quantify the non-normal spread in T_2^* values, we report the median value and the relative inter-decile range (RIDR):

$$\sigma_{\text{RIDR}} = \frac{D_{90} - D_{10}}{(\text{median})}, \tag{5}$$

where 80% of the measured values fall between the first decile D_{10} and the ninth decile D_{90}. In Fig. 4(a), the extracted $T_2^*\{\text{SQ}\}$ values have a median of 0.907(0.710, 1.03) μs, where the values in parentheses correspond to the deciles (D_{10}, D_{90}). As shown in Table I, the calculated RIDR for the extracted $T_2^*\{\text{SQ}\}$ values is 35%. We attribute the spatially correlated variations in $T_2^*\{\text{SQ}\}$ to axial stress gradients within pixels [13,16]. The observed stress features are likely due to polishing-induced imperfections in the substrate surface upon which the N-V^- ensemble layer is grown [25].

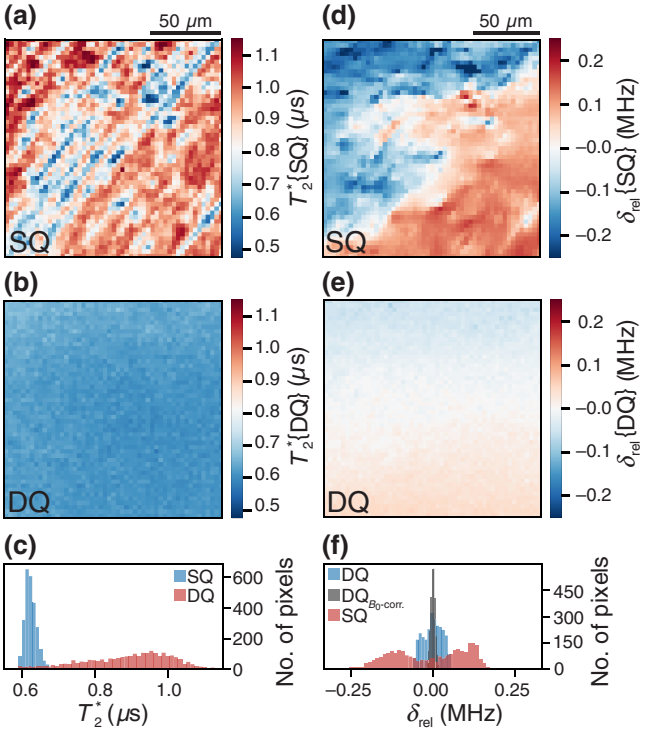


FIG. 4. Imaging the ensemble spin properties. (a) An image of the single quantum (SQ) T_2^* extracted by fitting the SQ 2-Ramsey fringe decay to Eq. (4). The field of view is 125 μm by 125 μm. The spatial variations in $T_2^*\{\text{SQ}\}$ are due to stress-induced broadening of the N-V^- resonances within the three-dimensional volume imaged onto a pixel. (b) An image of the double quantum $T_2^*\{\text{DQ}\}$ measured using the DQ 4-Ramsey protocol across the same field of view as shown in (a). In pixels with minimal stress gradients, the $T_2^*\{\text{DQ}\}$ is half the $T_2^*\{\text{SQ}\}$, as expected, due to the effectively doubled dipolar coupling to the surrounding paramagnetic spin bath, which dominates the N-V^- dephasing [16]. (c) A histogram of $T_2^*\{\text{SQ}\}$ and $T_2^*\{\text{DQ}\}$ values from the pixels in (a) and (b). (d) An image of the relative SQ resonance shifts $\delta_{\text{rel}}\{\text{SQ}\}$ from the median SQ Ramsey fringe frequency. The variations in $\delta_{\text{rel}}\{\text{SQ}\}$ are attributed predominantly to axial-stress-induced shifts of the N-V^- resonance frequencies between pixels. (e) An image of the relative DQ detuning $\delta_{\text{rel}}\{\text{DQ}\}$ across the same field of view as shown in (a), (b), and (d). The axial-stress-induced shifts apparent in (d) are mitigated. Inhomogeneity in the magnitude of the applied bias magnetic field B_0 results in a residual gradient of less than 1.4 μT. (f) A histogram of the extracted SQ and DQ δ_{rel} values from the pixels in (d) and (e). The distribution of DQ δ_{rel} values with the setup-specific B_0-gradient contribution corrected is shown in gray.

Invulnerable to within-pixel stress gradients, the measured $T_2^*\{\text{DQ}\}$ values are 5.6× more uniform than the $T_2^*\{\text{SQ}\}$ values, with a median of 0.621(0.605, 0.643) μs and an RIDR of 6.0%. Additionally, the median $T_2^*\{\text{DQ}\}$ is approximately one half the longest measured $T_2^*\{\text{SQ}\}$, 1.15(3) μs, as expected when stress-induced dephasing is

TABLE I. The median extracted fit parameters ($\tilde{x}$) using Eq. (4) for SQ and DQ Ramsey fringe imaging. The lower and upper deciles, D_{10} and D_{10}, are given in parentheses (80% of the pixels exhibit values between D_{10} and D_{90}). The SQ and DQ relative interdecile ranges (RIDR) calculated using Eq. (5) are included.

	SQ		DQ	
	$\tilde{x}$ (D_{10}, D_{90})	RIDR	$\tilde{x}$ (D_{10}, D_{90})	RIDR
Dephasing time, T_2^* (μs)	0.907 (0.710, 1.03)	35%	0.621 (0.605, 0.643)	6.0%
Fringe frequency, f_0 (MHz)	3.09 (2.94, 3.22)	...	6.00 (5.96, 6.04)	...
Fringe frequency, f_0 (B_0-corr.) (MHz)	3.10 (2.95, 3.21)	...	6.00 (5.99, 6.01)	...
Fringe amplitude, A_0 (D.U.)	72.1 (61.8, 76.6)	21%	73.5 (66.5, 77.0)	14%

negligible and the dominant contribution to T_2^* is dipolar coupling to an electronic spin bath (in this case of predominantly neutral substitutional nitrogen) [16].

B. Fringe frequencies

Figures 4(d)–4(f) display the extracted SQ and DQ Ramsey fringe frequencies associated with the detuning of the applied MW pulses from the spin transition frequency for the $m_I = 0$ hyperfine population. The relative detuning δ_{rel} from the median Ramsey fringe frequency f_0 is shown in Figs. 4(d)–4(f) to highlight the inhomogeneity across the field of view. The median SQ fringe frequency, $f_0\{\text{SQ}\}$, is 3.09 (2.94, 3.22) MHz. The absolute spread in $f_0\{\text{SQ}\}$, $|D_{90} - D_{10}| = 280(14)$ kHz, is comparable to the median N-V^- resonance line width and attributed to stress gradients spanning multiple pixels [13].

The DQ fringe frequencies exhibit a median $f_0\{\text{DQ}\}$ of 6.00 (5.96, 6.04) MHz. Note that the factor of 2 between the median detunings $f_0\{\text{SQ}\}$ (approximately 3 MHz) and $f_0\{\text{DQ}\}$ (approximately 6 MHz) is consistent with the doubled effective gyromagnetic ratio for the DQ sensing basis. The absolute spread in $f_0\{\text{DQ}\}$ is approximately 3.6× smaller than the spread in $f_0\{\text{SQ}\}$, with the remaining variation dominated by a quasilinear gradient of less than 1.4 μT due to residual inhomogeneity in the 5 mT applied bias magnetic field. In Fig. 4(f), a histogram of the relative shifts $\delta_{\text{rel}}\{\text{DQ}\}$ with a linear B_0-gradient contribution subtracted is included in gray and exhibits an absolute spread of $|D_{90} - D_{10}| = 20(1)$ kHz (approximately 13× smaller than the spread in $f_0\{\text{SQ}\}$).

C. Contrast

In the present work, the inhomogeneity in the measurement contrast C is largely independent of the choice of sensing basis (SQ or DQ) and is attributed to the Gaussian intensity profile of the excitation beam and fixed exposure duration. The extracted amplitudes A_i for the measured Ramsey fringes, which are proportional to C, are reported in digital units (D.U.) of accumulated difference as measured by the heliCam C3. The median amplitudes $A_0\{\text{SQ}\}$ and $A_0\{\text{DQ}\}$[72.1(61.8, 76.6) D.U. and 73.5(66.5, 77.0) D.U.] as well as the RIDR (21% and 14%) are comparable and are included in Table I. Images of $A_0\{\text{SQ}\}$ and $A_0\{\text{DQ}\}$ are provided in the Supplemental Material [24] for reference.

V. MAGNETIC SENSITIVITY ANALYSIS

We now compare the magnetic sensitivity of the SQ 2-Ramsey and DQ 4-Ramsey protocols across the same field of view described in Sec. IV. The narrower distribution of $T_2^*\{\text{DQ}\}$ and the resonance shifts $\delta_{\text{rel}}\{\text{DQ}\}$ translate into improved, more homogeneous magnetic sensitivity. For both sensing bases, we select an optimal free-precession interval τ and applied MW frequency (or frequencies) f_{mw} to maximize the median N-V^- response to a change in magnetic field, dS/dB (see Appendix B). Under these conditions, a series of measurements is collected and used to determine the magnetic sensitivity pixel by pixel.

The magnetic-field sensitivity is defined as $\delta B\sqrt{T_m}$, where T_m is the measurement duration and δB is the minimum detectable magnetic field, i.e., the field giving a signal-to-noise ratio (SNR) of 1 [28–31]. A measurement with duration T_m and sampling frequency $F_s = 1/T_m$ has a Nyquist-limited single-sided bandwidth of $\Delta f = F_s/2$. When the measurement bandwidth is sampling-rate limited, the minimum detectable magnetic field δB is given by the standard deviation of a series of measurements, σ_B. The sensitivity to fields within that bandwidth Δf can therefore be expressed as [32]

$$\eta = \sigma_B\sqrt{T_m} = \frac{\sigma_B}{\sqrt{2\Delta f}}. \tag{6}$$

In the present work, $F_s \approx 1.5$ kHz, set by the camera's external frame rate. Each external frame contains the accumulated difference signal of multiple Ramsey sequences acquired at an internal exposure rate of approximately 140 kHz (see the Supplemental Material [24]). The standard deviation of each pixel is calculated from 1250 consecutive frames (1 s of acquired data) and converted to magnetic field units using the calibration dS/dB measured for each pixel. Allan deviations of measurements using the SQ and DQ sensing bases are provided in the Supplemental Material [24]. Although the fixed time required to transfer

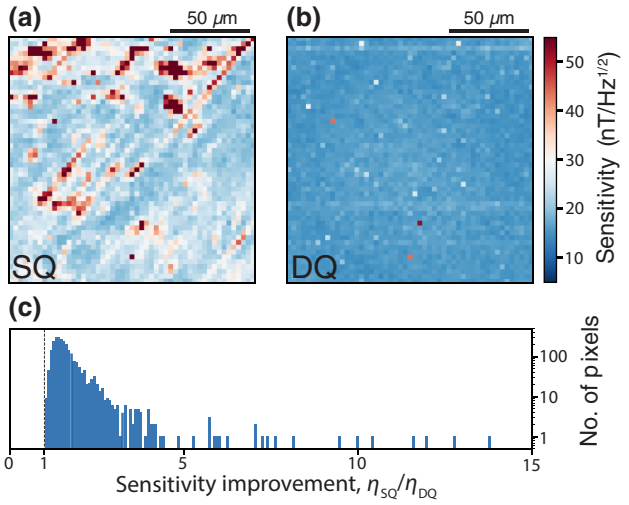


FIG. 5. Imaging the dc magnetic sensitivity. (a) The sensitivity image acquired with the SQ 2-Ramsey protocol when operating at an applied MW field f_{mw} and free-precession interval τ that optimize the median per-pixel magnetic sensitivity. (b) The sensitivity image acquired with the DQ 4-Ramsey protocol with optimal f'_{mw} and τ', across the same field of view as (a). A few isolated defective pixels with degraded sensitivity are visible. (c) A histogram of the improvement in the relative sensitivity $\eta_{\mathrm{SQ}}/\eta_{\mathrm{DQ}}$ per pixel.

data from the camera's 500-frame buffer (approximately 5 s, neglected in the above analysis) prevents continuous field monitoring at the calculated sensitivity for arbitrarily long times, the buffer still allows sets of high-bandwidth imaging data to be acquired over 0.4 s.

The resulting sensitivities η_{DQ} and η_{SQ} are plotted in Figs. 5(a) and 5(b). The median DQ 4-Ramsey per-pixel magnetic sensitivity $\eta_{\mathrm{DQ}} = 15(14,16)$ nT Hz$^{-1/2}$ provides a factor of about 1.5× improvement compared to the SQ 2-Ramsey per-pixel magnetic sensitivity, $\eta_{\mathrm{SQ}} = 22(19,34)$ nT Hz$^{-1/2}$ with voxel dimensions of $(2.5 \times 2.4 \times 1)$ μm^3. The upper and lower deciles, D_{10} and D_{90}, are reported in parentheses. The typical uncertainty in the calculated per-pixel magnetic sensitivity, about 6%, is dominated by the uncertainty in determining the parameters extracted from fitting the dc-magnetometry curve in each pixel.

The median (D_{10}, D_{90}) volume-normalized sensitivities are therefore $\eta^V_{\mathrm{DQ}} = 34(32,37)$ nT Hz$^{-1/2}$ μm$^{3/2}$ and $\eta^V_{\mathrm{SQ}} = 53(44,79)$ nT Hz$^{-1/2}$ μm$^{3/2}$. We observe about a 4.7× reduction in the RIDR for η_{DQ} (approximately 14%) compared to the RIDR of η_{SQ} (approximately 67%). The improved median sensitivity and reduced spread across the field of view are attributed to the elimination of axial-stress-induced dephasing and resonance shifts for the DQ 4-Ramsey protocol, such that it is possible to operate at the optimal τ and applied MW frequencies f_{mw} for an increased fraction of pixels simultaneously.

As illustrated in Fig. 5(c), all pixels exhibit improved magnetic sensitivity in the DQ sensing basis. Order-of-magnitude sensitivity improvements in the DQ basis are seen for the pixels corresponding to regions of diamond with higher stress gradients. In pixels with minimal stress-related effects, the improved magnetic sensitivity is attributed to (a) values of f_{mw} and τ that are more optimal for an increased fraction of the pixels (see Appendix B) and (b) the effectively doubled gyromagnetic ratio in the DQ sensing basis. The latter enables faster measurements (increased maximum F_s because $T_2^*\{\mathrm{DQ}\}$ and thus the optimal free-precession interval τ is reduced compared to $T_2^*\{\mathrm{SQ}\}$) for the same phase accumulation (see the Supplemental Material [24]). The residual 14% spread in η_{DQ} is a consequence of the Gaussian intensity profile of the excitation laser beam spot, which highlights the potential utility of optical beam-shaping techniques to enable further improvements.

The median volume-normalized magnetic sensitivity $\eta^V_{\mathrm{DQ}} = 34(32,37)$ nT Hz$^{-1/2}$ μm$^{3/2}$ demonstrated in this work coincidentally matches the value of 34 nT μm$^{3/2}$ Hz$^{-1/2}$ estimated in Ref. [33], which used photodiode-based cw-ODMR measurements to detect the single-neuron action potential from a living marine worm, *M. infundibulum*. Critically, the present work achieves a similar sensitivity while operating in an imaging modality, with degraded optical collection efficiency, and using N-V^- centers along only a single crystal axis; whereas the nonimaging apparatus employed in Ref. [33] overlapped the resonances from two N-V^- axes and had an approximately 16× higher optical collection efficiency.

VI. OUTLOOK

The demonstrated magnetic imaging method using the DQ 4-Ramsey protocol enables uniform magnetic sensitivity across a wide field of view independent of inhomogeneity in the host diamond material and the applied microwave control fields. In particular, the MW phase-alternation scheme of the 4-Ramsey protocol [Fig. 2(c)] isolates the double quantum magnetic signal from residual single quantum signal, decoupling the measurement from common-mode resonance frequency shifts induced by axial stress and temperature drift. The achieved 100× reduction in sensitivity to common-mode shifts is broadly advantageous, not only for magnetic imaging but also for single-channel applications such as magnetic navigation [34].

These methods provide a path toward imaging a range of dynamic magnetic phenomena, including nanotesla-scale fields from single mammalian neurons or cardiomyocytes, as well as fields from integrated circuits and condensed-matter systems. Increased optical excitation intensity and further diamond-material development could yield additional improvements in the volume-normalized magnetic sensitivity. Although pulsed magnetometry protocols favor

operating near the N-V^- center's saturation intensity ($1-3$ mW μm^{-2} [35]) to minimize the initialization and readout durations [3], this work achieves optimal sensitivity when operating at an average intensity approximately $45\times$ below saturation. The lower intensity allows the N-V ensemble to maintain a favorable charge state fraction by reducing optical ionization of N-V^- to N-V^0 [36,37]. For this reason, future material development to improve and stabilize the N-V charge fraction, for example by reducing the density of other parasitic defects that can act as charge acceptors [38], is critical.

The high-sensitivity pulsed imaging method demonstrated here also enables applications beyond broadband magnetic microscopy, such as parallelized high-resolution N-V^- ensemble NMR using ac-magnetic-field detection protocols. Additionally, the MW phase control utilized for the DQ 4-Ramsey protocol is sufficient to implement magnetically insensitive measurement protocols [39,40] as recently suggested by Ref. [41] for imaging the lattice damage induced by colliding weakly interacting massive particles (WIMPs).

ACKNOWLEDGMENTS

We thank John Barry for early efforts evaluating the heliCam C3 camera and technical insights, Heliotis AG for experimental assistance implementing the heliCam C3 camera; Pauli Kehayias, David Phillips, Wilbur Lew, Arul Manickam, Jeff Cammerata, John Stetson, and Micheal DiMario for valuable discussions; and Kevin Olsson for feedback on the manuscript. This material is based upon work supported by, or in part by, the U.S. Army Research Laboratory and the U.S. Army Research Office under Grant No. W911NF-15-1-0548; the Army Research Laboratory MAQP program under Contract No. W911NF-19-2-0181; the DARPA DRINQS program under Grant No. D18AC00033; the National Science Foundation (NSF) Physics of Living Systems (PoLS) program under Grant No. PHY-1504610; the Air Force Office of Scientific Research Award No. FA9550-17-1-0371; the Department of Energy (DOE) Quantum Information Science Enabled Discovery (QuantISED) program under Award No. DE-SC0019396; Lockheed Martin under Contract No. A32198; and the University of Maryland Quantum Technology Center. J.M.S. was supported by a Fannie and John Hertz Foundation Graduate Fellowship and a National Science Foundation Graduate Research Fellowship under Grant No. 1122374.

C.A.H., J.M.S., M.J.T., and E.B. conceived the experiments. C.A.H. and P.J.S. conducted the experiments. C.A.H. and J.M.S. analyzed the results. All authors contributed to and reviewed the manuscript. R.W. supervised the work.

APPENDIX A: EXPERIMENTAL DETAILS

An Agilent E9310A with built-in IQ modulation and a Windfreak SynthHD signal generator in combination with an external Marki-1545LMP IQ mixer provide the two-tone MW control fields and requisite phase control employed in this work. A Pulseblaster ESR-Pro with a 500 MHz clock controls the synchronization of applied MW pulses, optical pulses, and camera exposures (or photodiode readouts when applicable). Samarium cobalt ring-shaped magnets (as described in [16]) apply a 5 mT bias magnetic field used to split the $|0\rangle$ to $|\pm1\rangle$ transitions.

APPENDIX B: N-V^- ENSEMBLE MAGNETOMETER CALIBRATION

For the measurements in this work, the optimal free-precession interval τ and applied MW frequency f_{mw} are chosen to maximize the N-V^- response S to changes in magnetic field dS/dB (i.e., to minimize the sensitivity η). Although the optimal τ is approximately equal to T_2^* [3], the Ramsey-fringe beating introduced by the hyperfine splitting of the N-V^- restricts the possible choices of τ to discrete values. As a consequence, we select the nearest available τ to T_2^* for each sensing basis. With the free-precession interval τ fixed, the optimal f_{mw} is determined by sweeping the applied MW frequency to emulate a change in magnetic field, producing a dc-magnetometry curve from which f_{mw} is chosen to maximize the slope dS/dB. To determine the optimal MW frequencies for DQ Ramsey measurements, f'_{mw}, the two applied MW tones are swept differentially (one tone with positive detuning $+\delta$ and the second tone with an equal but opposite detuning $-\delta$). As with the SQ calibration, the values of f'_{mw} are chosen to maximize the N-V^- response dS/dB. For all measurements using the heliCam, the free-precession interval and MW frequency (or frequencies) are chosen to minimize the median per-pixel sensitivity across the field of view.

[1] L. Rondin, J. P. Tetienne, T. Hingant, J. F. Roch, P. Maletinsky, and V. Jacques, Magnetometry with nitrogen-vacancy defects in diamond, Rep. Prog. Phys. **77**, 056503 (2014).

[2] M. W. Doherty, N. B. Manson, P. Delaney, F. Jelezko, J. Wrachtrup, and L. C. L. Hollenberg, The nitrogen-vacancy colour centre in diamond, Phys. Rep. **528**, 1 (2013).

[3] J. F. Barry, J. M. Schloss, E. Bauch, M. J. Turner, C. A. Hart, L. M. Pham, and R. L. Walsworth, Sensitivity optimization for NV-diamond magnetometry, Rev. Mod. Phys. **92**, 015004 (2020).

[4] E. V. Levine, M. J. Turner, P. Kehayias, C. A. Hart, N. Langellier, R. Trubko, D. R. Glenn, R. R. Fu, and R.

L. Walsworth, Principles and techniques of the quantum diamond microscope, Nanophotonics **8**, 1945 (2019).

[5] D. R. Glenn, R. R. Fu, P. Kehayias, D. Le Sage, E. A. Lima, B. P. Weiss, and R. L. Walsworth, Micrometer-scale magnetic imaging of geological samples using a quantum diamond microscope, Geochem. Geophys. Geosyst. **18**, 3254 (2017).

[6] D. A. Simpson, J.-P. Tetienne, J. M. McCoey, K. Ganesan, L. T. Hall, S. Petrou, R. E. Scholten, and L. C. L. Hollenberg, Magneto-optical imaging of thin magnetic films using spins in diamond, Sci. Rep. **6**, 22797 (2016).

[7] J. M. McCoey, M. Matsuoka, R. W. de Gille, L. T. Hall, J. A. Shaw, J. Tetienne, D. Kisailus, L. C. L. Hollenberg, and D. A. Simpson, Quantum magnetic imaging of iron biomineralization in teeth of the chiton *Acanthopleura hirtosa*, Small Methods **4**, 1900754 (2020).

[8] J.-P. Tetienne, N. Dontschuk, D. A. Broadway, A. Stacey, D. A. Simpson, and L. C. L. Hollenberg, Quantum imaging of current flow in graphene, Sci. Adv. **3**, e1602429 (2017).

[9] M. J. H. Ku, T. X. Zhou, Q. Li, Y. J. Shin, J. K. Shi, C. Burch, L. E. Anderson, A. T. Pierce, Y. Xie, A. Hamo, U. Vool, H. Zhang, F. Casola, T. Taniguchi, K. Watanabe, M. M. Fogler, P. Kim, A. Yacoby, and R. L. Walsworth, Imaging viscous flow of the Dirac fluid in graphene, Nature **583**, 537 (2020).

[10] M. J. Turner, N. Langellier, R. Bainbridge, D. Walters, S. Meesala, T. M. Babinec, P. Kehayias, A. Yacoby, E. Hu, M. Lončar, R. L. Walsworth, and E. V. Levine, Magnetic Field Fingerprinting of Integrated-Circuit Activity with a Quantum Diamond Microscope, Phys. Rev. Appl. **14**, 014097 (2020).

[11] D. Le Sage, K. Arai, D. R. Glenn, S. J. DeVience, L. M. Pham, L. Rahn-Lee, M. D. Lukin, A. Yacoby, A. Komeili, and R. Walsworth, Optical magnetic imaging of living cells, Nature **496**, 486 (2013).

[12] D. R. Glenn, K. Lee, H. Park, R. Weissleder, A. Yacoby, M. D. Lukin, H. Lee, R. L. Walsworth, and C. B. Connolly, Single-cell magnetic imaging using a quantum diamond microscope, Nat. Methods **12**, 736 (2015).

[13] P. Kehayias, M. J. Turner, R. Trubko, J. M. Schloss, C. A. Hart, M. Wesson, D. R. Glenn, and R. L. Walsworth, Imaging crystal stress in diamond using ensembles of nitrogen-vacancy centers, Phys. Rev. B **100**, 174103 (2019).

[14] Z. Kazi, I. M. Shelby, H. Watanabe, K. M. Itoh, V. Shutthanandan, P. A. Wiggins, and K.-M. C. Fu, arXiv:2002.06237 (2021).

[15] I. Fescenko, A. Jarmola, I. Savukov, P. Kehayias, J. Smits, J. Damron, N. Ristoff, N. Mosavian, and V. M. Acosta, Diamond magnetometer enhanced by ferrite flux concentrators, Phys. Rev. Res. **2**, 023394 (2020).

[16] E. Bauch, C. A. Hart, J. M. Schloss, M. J. Turner, J. F. Barry, P. Kehayias, S. Singh, and R. L. Walsworth, Ultralong Dephasing Times in Solid-State Spin Ensembles via Quantum Control, Phys. Rev. X **8**, 031025 (2018).

[17] H. J. Mamin, M. H. Sherwood, M. Kim, C. T. Rettner, K. Ohno, D. D. Awschalom, and D. Rugar, Multipulse Double-Quantum Magnetometry with Near-Surface Nitrogen-Vacancy Centers, Phys. Rev. Lett. **113**, 030803 (2014).

[18] K. Fang, V. M. Acosta, C. Santori, Z. Huang, K. M. Itoh, H. Watanabe, S. Shikata, and R. G. Beausoleil, High-Sensitivity Magnetometry Based on Quantum Beats in Diamond Nitrogen-Vacancy Centers, Phys. Rev. Lett. **110**, 130802 (2013).

[19] P. Jamonneau, M. Lesik, J. P. Tetienne, I. Alvizu, L. Mayer, A. Dréau, S. Kosen, J.-F. Roch, S. Pezzagna, J. Meijer, T. Teraji, Y. Kubo, P. Bertet, J. R. Maze, and V. Jacques, Competition between electric field and magnetic field noise in the decoherence of a single spin in diamond, Phys. Rev. B **93**, 024305 (2016).

[20] M. S. J. Barson, P. Peddibhotla, P. Ovartchaiyapong, K. Ganesan, R. L. Taylor, M. Gebert, Z. Mielens, B. Koslowski, D. A. Simpson, L. P. McGuinness, J. McCallum, S. Prawer, S. Onoda, T. Ohshima, A. C. Bleszynski Jayich, F. Jelezko, N. B. Manson, and M. W. Doherty, Nanomechanical sensing using spins in diamond, Nano Lett. **17**, 1496 (2017).

[21] P. Udvarhelyi, V. O. Shkolnikov, A. Gali, G. Burkard, and A. Pályi, Spin-strain interaction in nitrogen-vacancy centers in diamond, Phys. Rev. B **98**, 075201 (2018).

[22] A. Barfuss, M. Kasperczyk, J. Kölbl, and P. Maletinsky, Spin-stress and spin-strain coupling in diamond-based hybrid spin oscillator systems, Phys. Rev. B **99**, 174102 (2019).

[23] F. Dolde, H. Fedder, M. W. Doherty, T. Nöbauer, F. Rempp, G. Balasubramanian, T. Wolf, F. Reinhard, L. C. L. Hollenberg, F. Jelezko, and J. Wrachtrup, Electric-field sensing using single diamond spins, Nat. Phys. **7**, 459 (2011).

[24] See the Supplemental Material at http://link.aps.org/supplemental/10.1103/PhysRevApplied.15.044020 for additional information on the N-V Hamiltonian, the DQ 4-Ramsey measurement protocol, and the magnetic imaging results.

[25] I. Friel, S. L. Clewes, H. K. Dhillon, N. Perkins, D. J. Twitchen, and G. A. Scarsbrook, Control of surface and bulk crystalline quality in single crystal diamond grown by chemical vapour deposition, Diam. Relat. Mater. **18**, 808 (2009).

[26] N. Bar-Gill, L. M. Pham, A. Jarmola, D. Budker, and R. L. Walsworth, Solid-state electronic spin coherence time approaching one second., Nat. Commun. **4**, 1743 (2013).

[27] A. Przybylski, B. Thiel, J. Keller-Findeisen, B. Stock, and M. Bates, GPUfit: An open-source toolkit for GPU-accelerated curve fitting, Sci. Rep. **7**, 15722 (2017).

[28] J. M. Taylor, P. Cappellaro, L. Childress, L. Jiang, D. Budker, P. R. Hemmer, A. Yacoby, R. Walsworth, and M. D. Lukin, High-sensitivity diamond magnetometer with nanoscale resolution, Nat. Phys. **4**, 810 (2008).

[29] D. Le Sage, L. M. Pham, N. Bar-Gill, C. Belthangady, M. D. Lukin, A. Yacoby, and R. L. Walsworth, Efficient photon detection from color centers in a diamond optical waveguide, Phys. Rev. B **85**, 121202(R) (2012).

[30] M. Bal, C. Deng, J. L. Orgiazzi, F. R. Ong, and A. Lupascu, Ultrasensitive magnetic field detection using a single artificial atom, Nat. Commun. **3**, 1324 (2012).

[31] R. S. Schoenfeld and W. Harneit, Real Time Magnetic Field Sensing and Imaging Using a Single Spin in Diamond, Phys. Rev. Lett. **106**, 030802 (2011).

[32] J. M. Schloss, J. F. Barry, M. J. Turner, and R. L. Walsworth, Simultaneous Broadband Vector Magnetometry Using Solid-State Spins, Phys. Rev. Appl. **10**, 034044 (2018).

[33] J. F. Barry, M. J. Turner, J. M. Schloss, D. R. Glenn, Y. Song, M. D. Lukin, H. Park, and R. L. Walsworth, Optical magnetic detection of single-neuron action potentials using quantum defects in diamond, Proc. Natl. Acad. Sci. U.S.A. **113**, 14133 (2016).

[34] A. Canciani and J. Raquet, Absolute positioning using the earth's magnetic anomaly field, Navig., J. Inst. Navig. **63**, 111 (2016).

[35] T.-L. Wee, Y.-K. Tzeng, C.-C. Han, H.-C. Chang, W. Fann, J.-H. Hsu, K.-M. Chen, and Y.-C. Yu, Two-photon excited fluorescence of nitrogen-vacancy centers in proton-irradiated type Ib diamond, J. Phys. Chem. A **111**, 9379 (2007).

[36] S. T. Alsid, J. F. Barry, L. M. Pham, J. M. Schloss, M. F. O'Keeffe, P. Cappellaro, and D. A. Braje, Photoluminescence Decomposition Analysis: A Technique to Characterize N-*V* Creation in Diamond, Phys. Rev. Appl. **12**, 044003 (2019).

[37] D. Aude Craik, P. Kehayias, A. Greenspon, X. Zhang, M. Turner, J. Schloss, E. Bauch, C. Hart, E. Hu, and R. Walsworth, Microwave-Assisted Spectroscopy Technique for Studying Charge State in Nitrogen-Vacancy Ensembles in Diamond, Phys. Rev. Appl. **14**, 014009 (2020).

[38] A. M. Edmonds, C. A. Hart, M. J. Turner, P.-O. Colard, J. M. Schloss, K. S. Olsson, R. Trubko, M. L. Markham, A. Rathmill, B. Horne-Smith *et al.*, Characterisation of CVD diamond with high concentrations of nitrogen for magnetic-field sensing applications, Mater. Quantum. Technol. **1**, 025001 (2021).

[39] D. M. Toyli, C. F. de las Casas, D. J. Christle, V. V. Dobrovitski, and D. D. Awschalom, Fluorescence thermometry enhanced by the quantum coherence of single spins in diamond, Proc. Natl. Acad. Sci. **110**, 8417 (2013).

[40] J. S. Hodges, N. Y. Yao, D. Maclaurin, C. Rastogi, M. D. Lukin, and D. Englund, Timekeeping with electron spin states in diamond, Phys. Rev. A **87**, 032118 (2013).

[41] S. Rajendran, N. Zobrist, A. O. Sushkov, R. Walsworth, and M. Lukin, A method for directional detection of dark matter using spectroscopy of crystal defects, Phys. Rev. D **96**, 035009 (2017).